Journal of Applied Geophysics 139 (2017) 1–15

Contents lists available at ScienceDirect

Journal of Applied Geophysics

journal homepage: www.elsevier.com/locate/jappgeo

Integration of geotechnical and geophysical techniques for the characterization of a small earth-filled canal dyke and the localization of water leakage

Grégory Bièvre [a,*], Pascal Lacroix [a,b], Laurent Oxarango [c], David Goutaland [d], Guy Monnot [e], Yannick Fargier [f]

[a] Univ. Grenoble Alpes, ISTerre, F-38000 Grenoble, France
[b] Univ. Grenoble Alpes, IRD, ISTerre, F-38000 Grenoble, France
[c] Univ. Grenoble Alpes, LTHE, F-38000 Grenoble, France
[d] CEREMA, Direction Territoriale Centre-Est, F-63017 Clermont-Ferrand, France
[e] CEREMA, Direction Territoriale Centre-Est, F-71405 Autun, France
[f] CEREMA, Direction Territoriale Normandie-Centre, F-41029 Blois, France

ARTICLE INFO

Article history:
Received 19 July 2016
Received in revised form 23 January 2017
Accepted 9 February 2017
Available online xxxx

Keywords:
Earth-filled canal dyke
Water head
Geometry
Leakage
Internal erosion
Geophysics

ABSTRACT

This paper investigates the combined use of extensive geotechnical, hydrogeological and geophysical techniques to assess a small earth dyke with a permanent hydraulic head, namely a canal embankment. The experimental site was chosen because of known issues regarding internal erosion and piping phenomena. Two leakages were visually located following the emptying of the canal prior to remediation works. The results showed a good agreement between the geophysical imaging techniques (Electrical Resistivity Tomography, P- and SH-waves Tomography) and the geotechnical data to detect the depth to the bedrock and its lateral variations. It appeared that surface waves might not be fully adapted for dyke investigation because of the particular geometry of the studied dyke, non-respectful of the 1D assumption, and which induced depth and velocity discrepancies retrieved from Rayleigh and Love waves inversion. The use of these classical prospecting techniques however did not allow to directly locate the two leakages within the studied earth dyke. The analysis of ambient vibration time series with a modified beam-forming algorithm allowed to localize the most energetic water flow prior to remediation works. It was not possible to detect the leakage after remediation works, suggesting that they efficiently contributed to significantly reduce the water flow. The second leakage was not detected probably because of a non-turbulent water flow, generating few energetic vibrations.

1. Introduction

Earth-filled canal embankments play several functions. Their role is to ensure shipping, water transport and water storage. Depending on their degree of impermeability, these dykes present the particularity of containing a more or less permanent hydraulic head. As such, they are prone to internal erosion phenomena, such as leakage and piping, which may lead to breaching (Foster et al., 2000; Fell et al., 2003). Furthermore, these structures might be older than several tens of years with very few available geotechnical data. Finally, these linear infrastructures may be stretched over up to several thousands of km per country (e.g. 9000 km of embankments in France according to the French Association of Embankments' Managers; france-digues.fr). As such, rapid and cost-effective methods are needed to assess the geotechnical conditions of these structures, to locate heterogeneous and/or weak zones and to optimize the location of geotechnical prospecting (drilling and in situ tests).

Since the pioneering works of Ogilvy et al. (1969) and due to technological improvements in the past decades, geophysical methods have been increasingly used to assess the geotechnical and hydrogeological setting of earth dykes. These methods have been used to characterize both the internal architecture of dykes (geometry, lateral variations, etc.) but also to try to localize specific anomalies such as internal erosion pipes. To achieve a first qualitative zoning, in terms of architecture and geometry, it is generally recommended to apply first rapid and efficient methods such as Slingram and/or Airborne ElectroMagnetic (AEM) induction techniques (Fauchard and Mériaux, 2007; Royet et al., 2013). When heterogeneous zones are detected, quantitative imaging techniques (among others: electrical resistivity, seismic refraction, ground-penetrating radar (GPR)) are then applied to try to locate in two dimensions (2D) defaults within the dyke (Fauchard and Mériaux, 2007; Niederleithinger et al., 2012). Among all geophysical techniques, Electrical Resistivity Tomography (ERT) is the most

* Corresponding author.
E-mail address: gregory.bievre@univ-grenoble-alpes.fr (G. Bièvre).

http://dx.doi.org/10.1016/j.jappgeo.2017.02.002
0926-9851/

commonly used to characterize dykes. It has been applied to image the depth to the substratum and its lateral variation (Cardarelli et al., 2010; Minsley et al., 2011; Cardarelli et al., 2014) as well as the internal variations or structures of dykes (Weller et al., 2006; Cho and Yeom, 2007). Time-lapse ERT has also been successfully used to image the internal evolution of dykes and to detect leakage and seepage path (Sjödahl et al., 2008; Sjödahl et al., 2009; Weller et al., 2014). On the one hand, the advantages of ERT are that the method is fast, easy to deploy and is sensitive to multiple parameters (among others, moisture and clay content) and to their change with time (Telford et al., 1990). On the other hand, the method suffers from non-uniqueness, which means that the images need to be calibrated with external information to produce a geotechnical interpretation (Telford et al., 1990). Among all other imaging techniques, there also exists a trade-off between depth and resolution. Another electrical method, namely Self Potentials, has been largely used on earth dykes. It is a passive electrical technique which was originally applied to the detection of leakage from water reservoirs by Ogilvy et al. (1969) and Bogoslovsky and Ogilvy (1970). Recently, Bolève et al. (2011) successfully localized seepages using Self Potentials completed with salt injection within the reservoir. Bolève et al. (2012) also used Self Potentials in parallel with hydro-acoustic measurements to detect and localize leakages within a dyke.

Seismic methods have been less used to characterize earth embankments. P-wave velocity (Vp) is highly sensitive to the water content and hence preferentially detects the water table within the dyke body (Ikard et al., 2015). Using P-wave refraction over a non-saturated earth dam, Kim et al. (2007) were able to locate low-velocity zones, which they associated to previously identified seepage entry path zones. P-wave refraction and/or tomography was also found to be adapted to locate the depth to the bedrock (Cardarelli et al., 2010). S-waves are less sensitive than P-waves to the presence of water. They also have the advantage of offering a better resolution than P-waves. S-wave velocity (Vs) imaging has however been poorly reported. This might be linked to the difficulty of generating energetic S-waves which results in a poor signal-to-noise ratio (SNR). Cardarelli et al. (2014) conducted both P- and S-waves tomography on an earth-filled dam which allowed them to evaluate the Poisson coefficient of the soil. Surface waves (SW) inversion has been recently applied for dyke characterization (Cardarelli et al., 2010; Cardarelli et al., 2014). It has been used preferentially to Vs imaging in order to retrieve vertical Vs profiles. Rayleigh SW offer the advantage of being recorded at the same time as P-waves, provided geophones with a sufficiently low cut-off frequency are used (Socco and Strobbia, 2004). SW inversion provides 1D Vs profiles where Vs varies only as a function of depth. The gathering of several 1D profiles spread along the dyke might allow an interpretation in terms of pseudo-2D Vs image. However, the 1D assumption might not be respected on dykes, considering the complex surface morphology of these structures when compared with a flat half-space. Karl et al. (2011) studied numerically these effects and concluded that they were insignificant for dykes with a base width-to-height ratio larger than four. Recently, the application of seismic ambient noise monitoring to a controlled laboratory-scale experiment and an in situ experiment allowed Planès et al. (2015) to detect significant velocity variations (a drop by around 20%) which they attributed to a piping process developing through a dam. Other techniques, such as acoustic emissions localization have been employed to localize leakages, using hydrophones (Bolève et al., 2012) or geophones on the dyke (Rittgers et al., 2015).

Other geophysical methods have also been applied for the location of pipes, voids and internal erosion paths within earth dykes. GPR was successfully applied to locate pipes and voids (Carlsten et al., 1995; Xu et al., 2010; Antoine et al., 2015) at several sites. However dykes generally contain clays and silts which prevent the systematic application of GPR.

The aim of this study is first to evaluate and compare the results obtained with classical active geophysical methods (refraction seismics, first arrivals tomography, electrical resistivity tomography) to characterize the geometry of a small (a few meters in height and width) earth-filled dyke with a permanent hydraulic head. The second objective is to test the ability of these methods to detect weak zones where known leakages take place. Remediation works on the chosen study site induced an emptying of the canal. This allowed to precisely locate the origin of the flows from within the canal. An extensive geotechnical prospecting, including drillings, in situ tests and laboratory tests, was conducted to calibrate the geophysical results. Finally, the third objective of this paper is to expose the results of leakage localization obtained with an ambient vibration measurement feasibility test. This test was not first designed to process ambient vibrations. It however provided promising results which will be presented in this paper.

2. Study site

The 56 km-long Canal de Roanne à Digoin (CRD) was built during the first half of the 19th century between 1830 and 1836. Its role is to ensure both shipping (freight and tourism) and water feeding to the "canal latéral à la Loire", a 200 km-long canal which allows to skip shipping on the Loire river, subject to floods and droughts. In the study area (Fig. 1a), the dyke of the CRD is made of a heterogeneous mixture of clays, silts, sands and gravels. It relies upon Jurassic marly limestones (Fig. 1b), the top of which is supposedly more or less weathered and decalcified (Bouiller et al., 1990). The dyke imperviousness is ensured by a concrete facing at the base of the canal (Fig. 1b). From a geometrical point of view, the dyke is 4 m wide on top and 18 m wide at its base, with a maximum height of 10 m. This corresponds to a base width-to-height ratio of around 1.8. The lateral slopes are 33° (3 horizontal units per 2 vertical units). An intermediate berm, towards the east and located between 1.5 m and 3 m below the dyke crest, serves as a road. The site was chosen because of known issues with regard to internal erosion phenomena, namely leakage and piping. A 5 m-long breach occurred in 2007 (Fig. 1c) 1.5 km south of the study site, which supposedly originated from internal erosion phenomena.

The study site is located in an area where two leakage zones were visually identified at the base of the dyke (Fig. 2). A 127 m long profile, covering two leakage zones (labelled LZ1 and LZ2 and located 34.5 m and 95 m along the profile, respectively) was specifically selected in order to test different geophysical and geotechnical methods (Fig. 2) between October 2010 and May 2011. The canal was emptied in November and December 2010 for improvement works. They allowed to precisely locate the flow inlets inside the dyke. They are referred to as leakage entry paths 1 (LEP1) and 2 (LEP2) in Fig. 2.

Fig. 3a and b show photographs of LZ1 and LZ2, respectively. Pictures were taken in October 2010 and the water height into the canal was 3.4 m. Pictures show that the pipes are pluridecimetric in diameter, with estimated flow rates of around 250 l/min for LZ1 (Fig. 3a) and of a few tens of l/min for LZ2 (Fig. 3b). Fig. 3c and d were shot in mid-November 2010, during the emptying of the canal and show photographs of LEP1 and LEP2, respectively. LEP1 is located 35.5 m along the profile. It is positioned at the base of the canal, 3.4 m below the top of the dyke and it is around 0.2 to 0.3 m in diameter. LEP2 is located 98 m along the profile. It is positioned around 1.5 m below the top of the dyke and it is also 0.2 to 0.3 m in diameter. The location of LEP and leakage zones are coincident between each other and, from a planimetric point of view, suggest a more or less straight path, from LEP1 to LZ1 and from LEP2 to LZ2, through the dyke (Fig. 2).

3. Investigation methods

This study included the performing of an extensive geotechnical investigation on the dyke, along with geophysical prospecting, over a period of 6.5 months. The location of the geotechnical and geophysical experiments is presented in Fig. 2. The time schedule of each experiment is exposed in Fig. 4 along with daily rainfall and hydrostatic levels in boreholes d1 and d3. Table 1 details the specifics of each experiment. Most geotechnical (drilling, coring, in situ and laboratory tests, nuclear

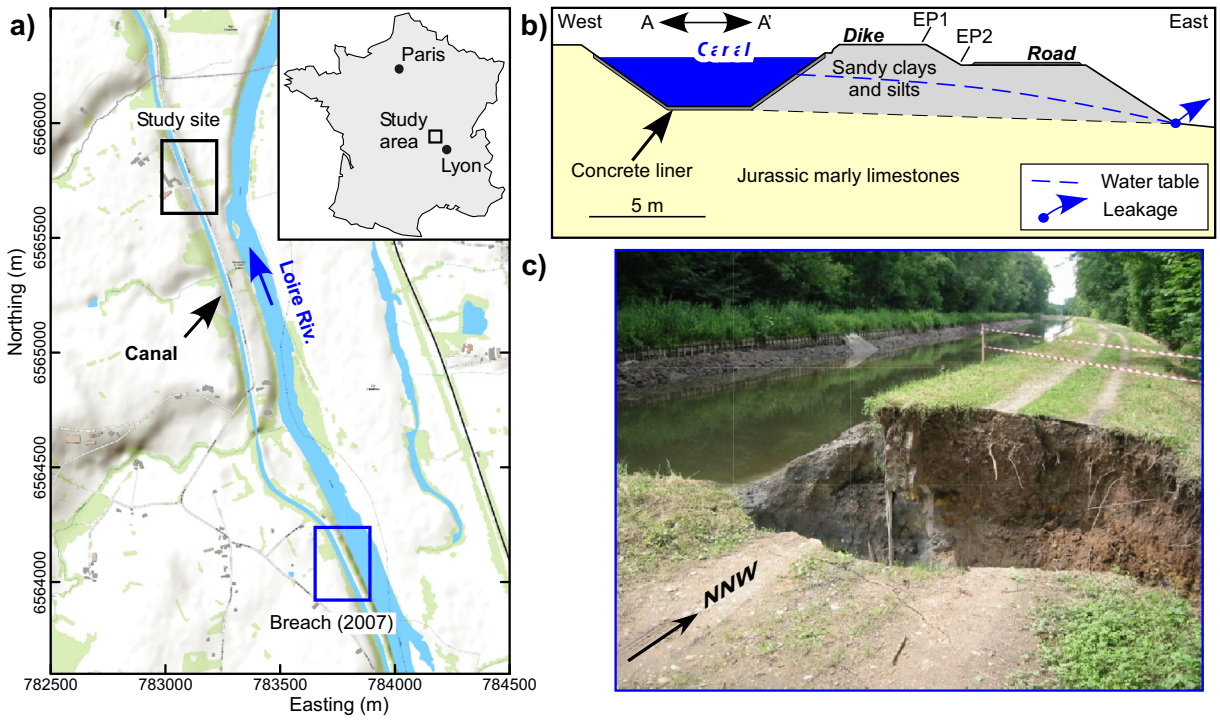

Fig. 1. Location and geotechnical context of the study area. a) Geographical location of the study site and of the breach which occurred in 2007. The topographic map comes from the ArcGis world imagery repository. Units are expressed in the Lambert93 French system. b) Schematic geotechnical cross-section AA′ of the dyke at the study site (location in Fig. 1a). c) Photograph of the breach which occurred in 2007 (location in Fig. 1a).

logging) and hydrogeological (piezometers) techniques are classical methods, the details of which can be found in reference books (e.g. Clayton et al. (1995). Only the geophysical and less classical geotechnical techniques will be further described in detail.

3.1. Geotechnics

Experiments started with three drillings (d1 to d3) in late October 2010. d1 (location in Fig. 2) is located at a distance of 69 m along the profile. It was drilled to a depth of 6.7 m with the objective of detecting the top of the non-weathered bedrock. It was further equipped with a permanent hydrostatic pressure probe set at a depth of 4.2 m, immediately above the interface separating the weathered bedrock from the base of the dyke. d2 is located at a distance of 65 m along the profile. It was augered down to a depth of 5.6 m and dyke materials were sampled each 0.5 m for further laboratory geotechnical identification. d3 is 7 m-deep and is located at a distance of 65 m along the road, 1.8 m below the top of the dyke (location in Fig. 2). It was equipped with an open piezometer casing. Two electrical profiles (EP1 and EP2) and one seismic profile (SP1) were conducted in November 2010. Their analysis allowed to determine the location of further drilling operations. In April 2011, three permeability and penetrometer tests were conducted in boreholes (p1 to p3). Finally, a 5.9 m-deep drilling (labelled C) was cored in April 2011. Neutron and gamma-gamma (γ-γ) logging were used to determine the moisture content and the density, respectively, along a specific drilling in the immediate vicinity of coring C. It is

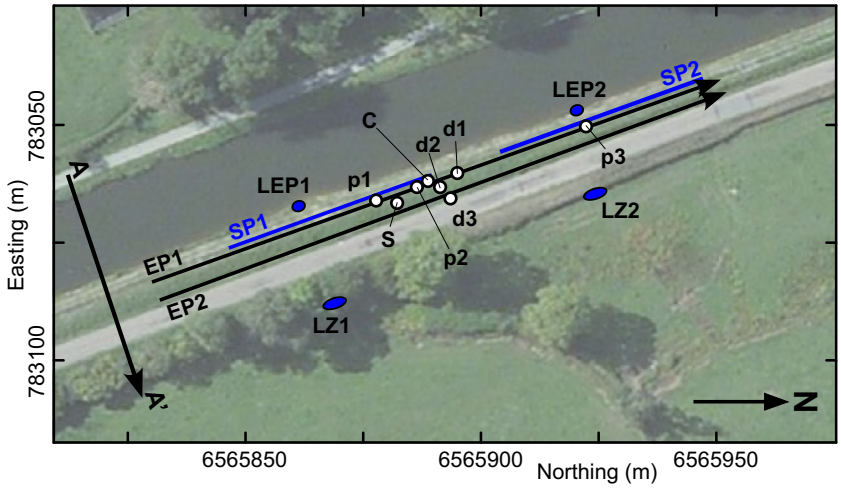

Fig. 2. Location of the geotechnical and geophysical experiments on the study site. The position of the 2 leakage entry paths (LEP1, LEP2) within the canal and of the 2 corresponding leakage zones (LZ1, LZ2) at the bottom of the dyke is also indicated. The location of cross-section AA′ (Fig. 01b) is indicated. The orthophotographic image comes from the ArcGis world imagery repository. Units are expressed in the Lambert93 French metric system. Details of the experiments are provided in Table 1.

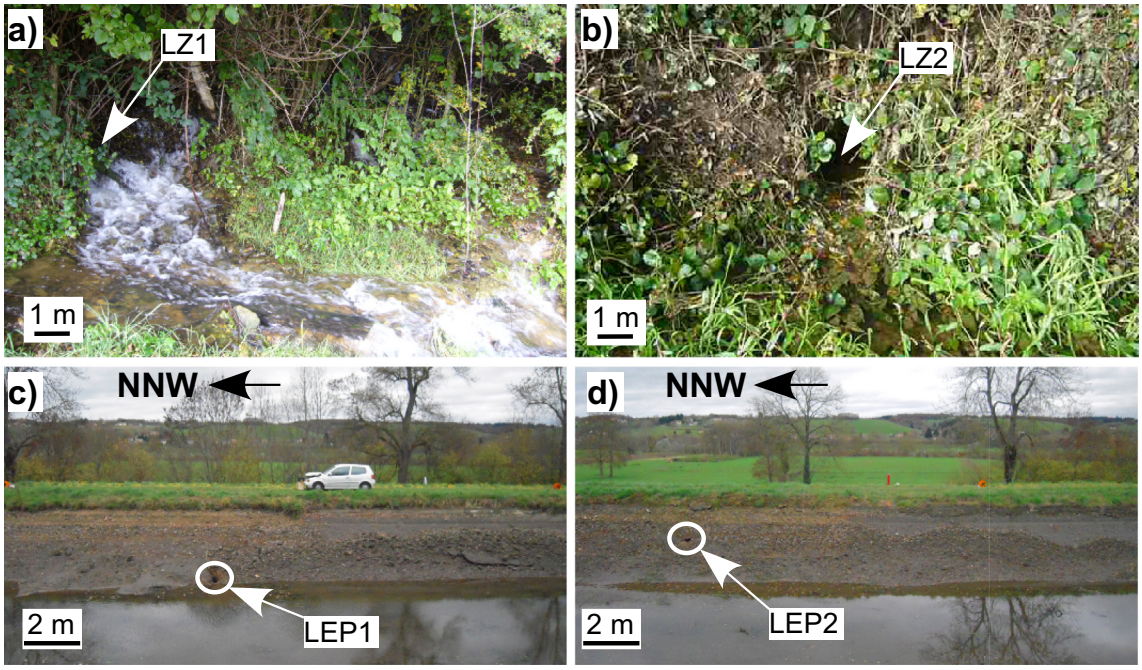

Fig. 3. photographs of the leakage zones and of the pipeholes within the dyke (location in Fig. 2). a) and b) Leakage zones LZ1 and LZ2, respectively; c) and d) leakage entry paths LEP1 and LEP2, respectively.

labelled C for convenience. Natural radioactivity logs, related to the clay content, were conducted in several boreholes (C, d1, d3). Finally, seismic profile SP1 was conducted again in mid-May 2011.

In situ scissometer (labelled S in Table 1 and in Figs. 2 and 4) tests consist of pushing a four-bladed vane into the soil and, at specific depths, rotating the vane from the rig located at surface. Once the test is over, the vane is pushed down to another depth. It is used to obtain the peak undrained shear strength and the remoulded undrained shear strength of the ground (Clayton et al., 1995).

Permeability and Penetrometer tests were conducted using an almost continuous hydraulic profiling tool called Perméafor. It was developed in France in the 1990s (Ursat, 1992) and was improved in the past decade (Reiffsteck et al., 2010). It was recently applied to an earth embankment along with GPR (Antoine et al., 2015). Basically, a porous tip and a penetrometer mounted on the same rig are driven into the ground by increments of 0.2 m. The injection is done continuously along the 0.2 m increment. Penetration is then stopped and the water flow is recorded during 10 s over a period of 10 to 30 s. Penetration then starts again for a new 0.2 m increment. The hydraulic parameter *Pk* derived from this test is equivalent to permeability and is expressed as (1):

$$P_k = \frac{Q}{H'} \tag{1}$$

where:
P_k is the derived parameter (m^2/s),
Q is the measured water ouflow (m/s).
H' is the corrected water head (m^{-1}).
P_k is then related to the hydraulic conductivity using the following relationship (2):

$$K = \alpha \cdot P_k \tag{2}$$

Where K is the hydraulic conductivity (m/s) and α is a shape factor due to the tip (m^{-1}) with a value around 2.8 (Reiffsteck et al., 2010).

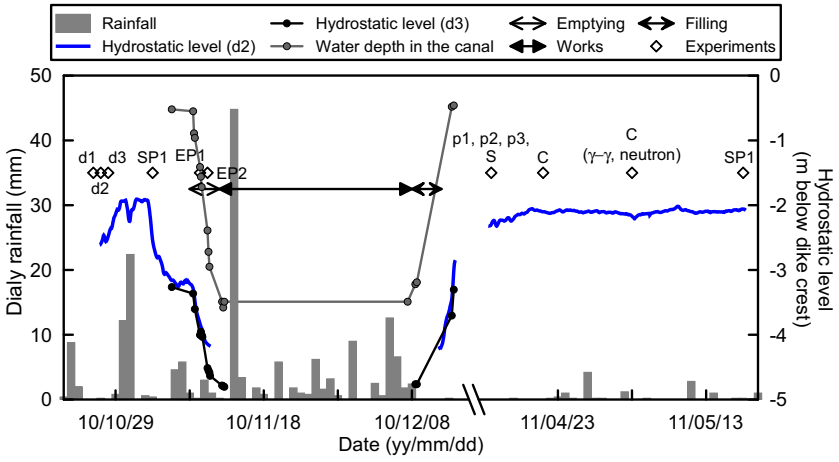

Fig. 4. Dates of the experiments with their associated environmental and hydrological conditions. The dashed part of the hydrostatic level in d1 indicates a water level below the position of the cell within the dyke (4.2 m below ground level).

Table 1
Characteristics of the geotechnical and geophysical experiments.

Experiment	Distance along Profile (m)	Date	Characteristics
d1	69	26 October 2010	6.7 m-deep drilling equipped with a permanent hydrostatic pressure probe set at 4.2 m below ground level Gamma-ray logging
d2	65	27 October 2010	5.6 m-deep auger drilling with soil sampling each 0.5 m and equipped with temperature probes
d3	65	28 October 2010	7 m-deep drilling equipped with an open piezometer casing Gamma-ray logging
SP1	18 to 64	03 November 2010	24, 4.5 Hz, vertical and horizontal geophones, 2 m apart.
EP1	0 to 127	09 November 2010	128 electrodes 1 m apart, Wenner-Schlumberger configuration, 3567 measurements
EP2	0 to 127	10 November 2010	128 electrodes 1 m apart, Wenner-Schlumberger configuration, 3471 measurements
S	55	14 April 2011	Borehole scissometric (vane) tests
p1, p2, p3	51, 60, 99	19 and 20 April 2011	Permeability and penetrometer tests in drilling
C	62	21 April 2011	5.9 m deep coring with gamma-ray logging
C		03 May 2011	Nuclear logging (gamma-gamma and neutron-neutron)
SP1	18 to 64	18 May 2011	24, 4.5 Hz, vertical and horizontal geophones, 2 m apart.

3.2. Seismics

A 46 m long seismic profile, labelled SP1 in Fig. 2, was conducted with 24 geophones spread each 2 m. This profile, which centre was located above LZ1, was first acquired in November 2010, before remediation works, and was repeated in May 2011 after repairs. Compressional (P) and shear (S) waves were recorded with 4.5 Hz, vertical and horizontal geophones, respectively. P-waves were generated with a 5 kg sledgehammer vertically hitting a metallic plate on the ground. S-waves were generated with the same sledgehammer horizontally hitting a loaded plank oriented perpendicular to the profile. For P and S-waves, respectively, 12 and 14 sources regularly spread along the profile allowed to pick 272 and 320 first arrival times with an uncertainty estimated at 0.25 ms. 4 offset shots at each end were further acquired for Rayleigh waves investigation.

P-wave velocity (Vp) and S-wave velocity (Vs) were first deduced from a classical refraction study. First arrival times were then inverted using the iterative Ra2dTomo code (Günther and Rücker, 2006) which uses unstructured triangular meshes. Minimum and maximum velocity values deduced from the refraction interpretation were used to estimate velocity bounds. The L1 norm was used to sharpen the transition between adjacent units. Acceptable errors with root mean-square (RMS) errors below 1.5×10^{-3} s were reached after a few iterations.

Surface waves were also recorded during the campaign. Rayleigh and Love-waves, from P-wave and S-wave measurements respectively, were processed with the Geopsy package available at www.geopsy.org (Wathelet et al. (2004). The dispersion curves for the fundamental modes from a group of around eight geophones were first computed using the frequency-wavenumber (*f-k*) method (Socco and Strobbia, 2004). Dispersion curves were then inverted using the Neighbourhood Algorithm (Socco and Strobbia, 2004; Wathelet, 2008) with parametrization constraints deduced from the refraction and tomographic studies.

Finally, ambient seismic noise was recorded during 1 min with the 4.5 Hz vertical geophones along profile SP1 in November 2010 before works and in May 2011, after works. These recordings (sampling frequency $fs = 250$ Hz) were conducted for feasibility tests. The main objective was to evaluate the possible strong energetic content of the seismograms located just above the leakage path relative to the others. It was hypothesized that the possible strong seismic vibrations recorded during monitoring measurements would originate from the water circulating through the dam. This feasibility test however provided useful and promising results which will be exposed in Section 4.4. The processing of the one minute-long dataset along SP1 is described further.

Data were first analysed in terms of direction of propagation. Assuming a radial propagation from a source at depth and directed towards each end of the seismic profile, velocity and directions of propagation were analysed in the *f-k* domain. In order to locate the source of vibration at depth (and hence, the pipe), beam-forming methods were then tested on the seismic traces of the array. The technique used is adapted from the method developed for the location of micro-earthquakes and rockfalls within a rockslide (Lacroix and Helmstetter, 2011) or for snow avalanche location (Lacroix et al., 2012). This method searches the source position and the wave velocity that maximizes the average intertrace correlation (C) after shifting traces in time by their travel time (Fig. 5a), weighted as a function of their inter-distance (see Lacroix and Helmstetter (2011). The algorithm searches for a continuous correlation over the whole seismic network (i.e. the 24 geophones).

The algorithm was adapted to also take into account the geometrical attenuation of the signal amplitude with the distance to the source d. This decay is a function of $d^{-1/2}$ for surface wave and d^{-1} for body waves (Aki and Richards, 1980). The algorithm searches for the source location that minimizes the residuals (noted ε) between the recorded amplitudes (defined as the maximum amplitude of each trace over the time window δ), and the modelled amplitude (defined as $a + b.R^{-\alpha}$, with $\alpha = 0.5$ or 1 and a,b are the inverted coefficients in the least-square sense). Fig. 5b presents the maximum amplitude of each trace for the 2 s time-window of Fig. 5a as a function of the distance from the source. These data were fitted using a decay function in d^{-1} and $d^{-1/2}$. The relative root mean square errors are 60% (d^{-1}) and 76% ($d^{-1/2}$). These high errors may have several origins: the investigated structure is not a half-space, it is stratified and there is also a water table, the source is located in the near-field with respect to the closest geophones (inducing correlations with a mixture of body and surface waves). The weight of the amplitude for the inversion is described further. The two indicators (C and ε) were then combined into a single one Λ, using a coefficient of proportionality β:

$$\Lambda(x,z,V) = C(x,z,V) + \beta/\varepsilon(x,z) \quad (3)$$

Coefficient β gives the relative importance of the phase and the amplitude in the search position. It is fixed after a process of trial and errors. In the present case, it was decided to give more weight to the signal phase than its amplitude. β was fixed so that the second term (β/ε) was approximatively 5% of the first term (C). Practically, the signals were first low-pass filtered (50 Hz) to focus on their most energetic part. They were then cut into windows of length δ (typically 2 s in this work). For each window, the source position and velocity along the trace and at depth, where Λ is maximum, was calculated. This inversion was first performed using a grid search spaced every 1 m along the x and z axis, a velocity of 100 m/s, before an optimization based on a Nelder-Mead algorithm (Nelder and Mead, 1965).

This process lead to one optimum location and one wave velocity per time-window δ. Since the source was not moving within the 1 min-long signal, it was possible to define the global probability density function (PDF) of $\Lambda(x,z,V)$ as the mean of all Λ calculated over each time-window δ. Two types of uncertainties on the results were then defined.

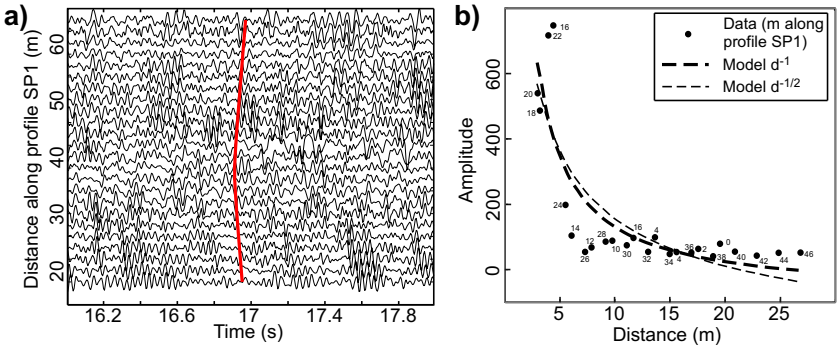

Fig. 5. Different steps of the source location algorithm. a) Average intertrace correlation calculated after travel time shift for a 2 s time-window. b) Maximum amplitude of the seismogram as a function of the distance from the source.

The first type was based on the dispersion of the series of best location found at each time window. The second type was based on the size of the global distribution (see Lacroix and Helmstetter, 2011): the standard deviation was calculated for all the locations displaying a value of $\Lambda(x,z) > 99\%$ of the maximum of $\Lambda(x,z)$.

As the parameters (δ, w) change, the dispersion around the median values evolves following a step-like pattern (Fig. 6). Therefore, the optimum values of the parameters were chosen on the sloping edge of these distributions, that is $\delta = 2$ s (Fig. 6a) and $w = 2$ m (Fig. 6b). These choices were based on two criteria: (1) consistent locations from a time-window to another one (reduced uncertainty), (2) intertrace weights as large as possible. The standard deviation is 0.5 m in the horizontal distance and 0.6 m in depth when δ varies, 0.5 m and 0.4 m when w varies. This confirms the robustness of the algorithm. Finally, the length of the time-window δ is similar to what was used for other source signals: rockfalls (Lacroix and Helmstetter (2011) or snow avalanches (Lacroix et al., 2012). Similarly, the value of the intertrace distance w is consistent with what was previously observed in another geological setting (Lacroix and Helmstetter, 2011).

3.3. Electrical resistivity tomography (ERT)

Electrical resistivity measurements were conducted at the top of the dyke along profile EP1 (location in Fig. 2) with 128 permanent electrodes 1 m apart. A second profile labelled EP2 (location in Fig. 2) with 128 electrodes 1 m apart was also conducted along the road, around 1.8 m below the dyke crest. The Wenner-Schlumberger array was chosen, as it provides both a good signal-to-noise ratio and good vertical and lateral resolution (Telford et al., 1990). Measurements were conducted with one initial sequence of 64 electrodes and 5 further roll-along sequences to cover the 127 m-long profile. Up to 3560 points were acquired for each profile. With this configuration and with respect to the ground resistivity (maximum of 200 to 300 $\Omega \cdot m$), the depth of investigation is estimated around 10 to 15 m.

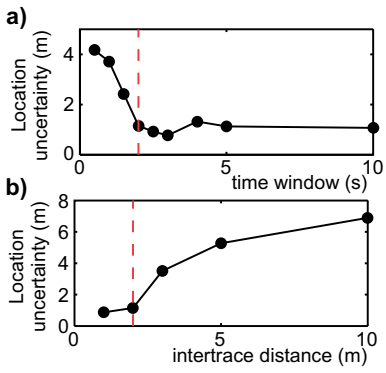

Fig. 6. Sensitivity of the source error location (1σ) a) to the length of the time window δ and b) to the intertrace-weight.

Apparent resistivity data were inverted with the Boundless Electrical Resistivity Tomography (BERT) algorithm developed by Günther et al. (2006) and Rücker et al. (2006). Data were reweighted using the L1 norm. The regularisation strength lambda (λ) was manually determined using a trial and errors approach to get a final Chi^2 value around 1, indicating that the data were fitted within a default measurement error of 3%. Relative RMS errors are below 5%.

4. Results

4.1. Geotechnical results

Most of the drillings and of the geotechnical tests were located in the vicinity of the most important leakage zone LZ1, between 50 m and 70 m along the SSE-NNW oriented profile, except for *P*3 which was conducted at a distance of 99 m, close to LZ2. Fig. 7 presents the geotechnical (Fig. 7a) and hydrological (Fig. 7b) tests, respectively, along with the geotechnical correlations and interpretation. Three geotechnical units have been visually identified in coring C (Fig. 7a). The first layer (unit 1) below ground has a thickness of 3 m to 4.2 m from the beginning to the end of the profile. It deepens regularly towards NNW, except at 65 m (drilling d2) where it locally reaches a depth of 4.6 m. Unit 1 is made of sandy clays-silts and sand (60–65% clays-silts and 30–40% sand) with a very slight increase in gravel content (from around 5% to 10%) in the first metre below ground, as shown in Fig. 8a.

Below unit 1, a second layer (labelled unit 2 in Fig. 7) is made of silty clays and sand. The granulometric distribution indicates a higher clay and silt content than unit 1 and shows a less regular thickness. It globally dips towards NNW along with an increase in thickness, from 0.6 m at the beginning of the profile (borehole p1; Fig. 7a) to 2.6 m in d2 and to 1.4 m in p3. These two units form the dyke itself and appear very slightly different in terms of geotechnical properties.

Penetration sounding curves (p1 to p3 in Fig. 7a) are expressed in slowness (time taken to penetrate 0.2 m vertically into the ground). p2 and p3 show a progressive increase in slowness from 0 s/0.2 m at surface to 10 s/0.2 m at the base of the dyke, indicating an increase in stiffness and/or density with depth. This interpretation is consistent with the progressive decrease in γ-γ count ratio in C, which indicates a progressive increase in the ground density.

In the context of the study site (dyke body and carbonate substratum), gamma-ray values are indicative of the global clay content (Telford et al., 1990) and are expressed in count/s (c/s). Gamma-ray logging in boreholes C and d1 show mean values of 60 c/s within the dyke body for both units. Between 4.7 m and 5.9 m deep in d1, gamma-ray values show a progressive decrease from 60 c/s to around 20 c/s. Below 5.9 m deep, gamma-ray values are around 20 c/s and could reflect the marly limestones. Between 5.9 m and 4.7 m, the progressive

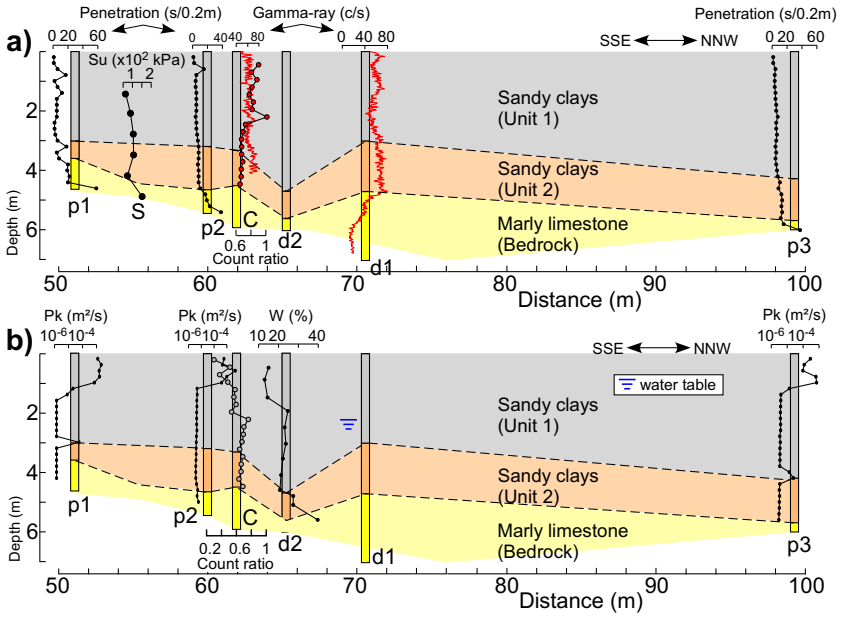

Fig. 7. a) Geotechnical and b) hydrological cross-sections between 50 m and 100 m along the profile. The details of drillings and experiments are provided in Table 1.

increase could correspond to the progressive weathering (and, hence, clay enrichment) of the top of the jurassic marly limestone.

Fig. 7b presents the hydrological cross-section along the studied profile. Permeability logging in p1 to p3 shows that, below a depth between 1 and 1.5 m, the dyke exhibits very low permeability (Pk around 1×10^{-6} m^2/s). A striking figure is the very large increase in permeability at 3 m depth in p1 and at 4.2 m depth in p3. This depth coincides with the interface between units 1 and 2. In agreement with (Fell et al., 2003), this suggests that lithological and/or geotechnical discontinuities within embankment dams constitute preferential flowpaths for water infiltration, leading to internal erosion and piping. This also supports the geotechnical interpretation in terms of 2 units, even if they exhibit very few geotechnical contrasts.

The water content profiles obtained by neutron logging in C (May 2011 the 03rd) and from soil sampling in d2 (October 2010 the 10th) are in agreement. They both show a stiff increase of water content in the vadose zone above the water table located at a depth of 2.1 m and 2 m, respectively. This is also in agreement with the permanent pressure cell in d1 which indicates a water table at a depth of 2.1 m (Fig. 4). Even if the sampling step in d2 is relatively coarse, the water table location is consistent for the 3 methods. Furthermore, and even if unit 1 is composed of fine materials, no evidence of a significant capillary fringe is found since the saturated moisture content level (from W and neutron count ratio) corresponds to the piezometric level in d1. Below, the saturated ground shows a progressive decrease in water content as the progressively decreasing γ-γ count ratio indicates an increase in density (Fig. 7a). At the bottom of d2, however, the water content shows a dramatic increase from 20% to 40% (Fig. 7b). This point will be discussed further.

Fig. 8 presents the results of laboratory identification tests, namely the granulometric analysis (Fig. 8a) and the methylene blue value of the soil (VBS) along with the water content in borehole d2 (Fig. 8b). Unit 1, from the surface down to 4.6 m deep is made of silts and clays (60–65%), sand (30–40%) and gravel (around 5%), the first metre below ground being slightly enriched in gravel (10–15%). Unit 2, below 4.6 m depth, is made of silts and clays (70%), sand (25–30%) and gravel (< 5%). This unit is enriched in silts and clays compared to unit 1. This is confirmed by VBS tests which indicate an argilosity below 3.2 for unit 1 and of around 4 for the bottom of unit 2. These tests confirm the slightly finer grain size of unit 2. They also allow to explain the higher water content at the bottom of d2 (Fig. 8b).

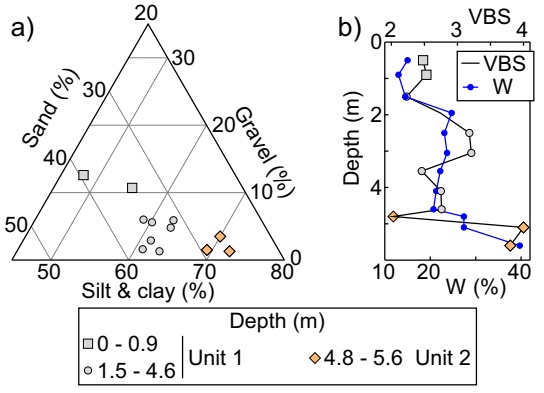

Fig. 8. Geotechnical tests on 12 samples from drilling d2 (location in Fig. 2). a) Granulometry. b) Methylene blue value of the soil (VBS) and water content (W) of samples from drilling d2 (location in Fig. 2). (For interpretation of the references to colour in this figure legend, the reader is referred to the web version of this article.)

4.2. Active geophysical prospecting

4.2.1. Seismics

Fig. 9a and b show the seismograms recorded along SP1 for a shot at the first geophone (abscissa 18 m). P- and S-waves are clearly distinguishable from Rayleigh (R) and Love (L) surface waves, respectively. Fig. 9c and d present the time-distance graphs with two end-shots and a central-shot for P- and S-waves, respectively. They both exhibit a two-layers subsurface. Below a superficial layer of low velocity (Vp = 300 m/s and Vs = 150 m/s), Vp increases to 2500–2700 m/s and Vs increases to 1200 m/s.

First arrivals were then inverted to produce a 2D image of the seismic velocities and the results are presented in Fig. 10. P-wave velocity image (Fig. 10a) indicates a two layers model with a sub-horizontal interface, in agreement with the refraction study (Fig. 9c). Low velocity levels (300 m/s) are found at surface, on a thickness of around 2 m. They overlay higher velocity levels (>1500 m/s and up to >3000 m/s). The first level could correspond to the unsaturated part of the dyke whereas the underlying faster levels could correspond to the saturated part of the dyke and to the bedrock. This interpretation is supported

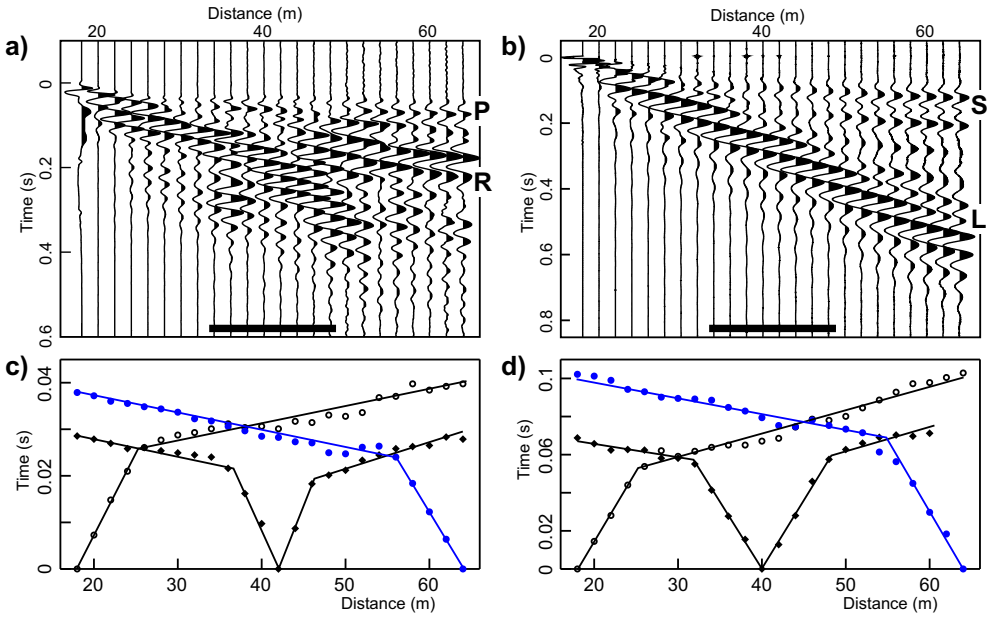

Fig. 9. Refraction study conducted in November 2010 along profile SP1 (location in Fig. 2). a) and b) Seismograms recorded for an end-shot at the first geophone of the profile and for the study of P-waves and S-waves, respectively. P: P-waves; R: Rayleigh waves; S: S-waves; L: Love waves. Bold bars represent the group of 8 geophones used for surface waves inversion. c) and d) Travel-time curves for two end-shots and a central shot, and for P- and S-waves, respectively.

by water pressure measurements in borehole d1 (70 m along the profile), which indicate the water table at a depth of 2.1 m below ground during measures. The superimposition of drillings on the image of Vp also indicates that it is difficult to establish a correlation between the lithological data and Vp because the lithological interfaces are located within the saturated part of the ground.

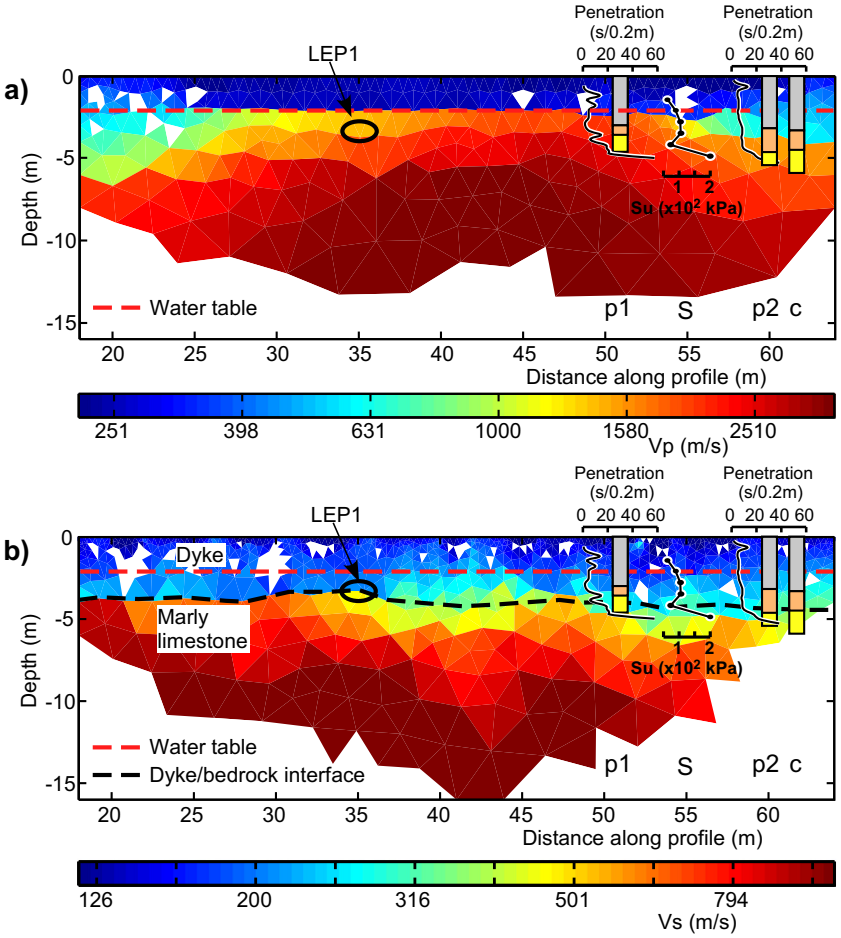

Fig. 10. Seismic travel-time tomography of profile SP1. a) Vp. b) Vs. White parts within images indicate regions not crossed by rays. Drillings and in situ tests are located in Fig. 2.

S-waves provide a better resolution than P-waves and offer the advantage of being less influenced by the presence of water. The resulting tomogram (Fig. 10b) indicates the presence of two layers. The upper layer has a velocity of around 150 to 300 m/s. Its thickness progressively increases from the beginning (3.5 m) to the end (5 m) of the profile. These low velocity levels correspond to the dyke itself (as confirmed by gamma-ray logging within boreholes; Fig. 7b). On the Vs image, it is not possible to distinguish between the two geotechnical units of the dyke (units 1 and 2; Fig. 7), probably because of a low mechanical contrast between them. Furthermore, the reduced thickness of unit 2 (1 to 1.5 m) with respect to geophone spacing (2 m) and to the expected resolution might prevent its detection. Higher velocities (up to 1200 m/s and more) are found below the dyke body and indicate the jurassic marly limestone. From abscissa 35 m to the end of the profile, the Vs contrast between the dyke and the bedrock appears less sharp. Noticeably, a relatively low-velocity zone (around 500 m/s) is observed between 35 m and 45 m in the upper part of the bedrock. This zone is well correlated with the first leakage zone and could indicate that water circulation takes place within a mechanically altered part of the top of the marly limestone at the interface with the dyke body. The superimposition of the drillings and of the geotechnical tests on the Vs image shows a very good agreement between these data (Fig. 10b). Vs dramatically increases below the interface between the dyke body and the marly limestone. In the same way, penetration tests p1 and p2 and scissometer test S show a sudden increase of the mechanical characteristics of the ground below this limit. This interface was picked along the whole profile (black dashed line in Fig. 10b) and was used as a priori information for the inversion of electrical profile EP1 (see Section 4.2.2).

Finally, the Poisson's ratio was estimated from P- and S-wave velocity. A value of around 0.33–0.36 was found in the unsaturated part of the dyke, which is typical of unsaturated silts. Poisson's ratio values of 0.44 to 0.49 were found for the saturated part of the dyke for the bedrock. These values are also typical of saturated formations.

Surface Rayleigh and Love waves were acquired at the same time that P and S-waves, respectively (seismograms are presented in Fig. 9a and b). Dispersion analysis were carried out for two end-shots and one group of eight geophones (located in Fig. 9a and b) along profile SP1. The analysis of the f-k spectrum for Rayleigh waves along with the spectral amplitude (Fig. 11a) shows that most of the energetic propagation occurs in modes higher than the fundamental mode, between 15 Hz and 35 Hz. This might probably result from diffraction and/or wave splitting effects caused by the particular geometry of the dyke (Fig. 11a; Cardarelli et al. (2010)

On the contrary, Love waves show a high-energetic fundamental mode between 10 Hz and 30 Hz (Fig. 11b). The mean dispersion curve for two end-shots and the associated standard deviation were calculated and they are presented in Fig. 11c. Several parametrizations were tested, noticeably with two and three layer models and/or an increase in Vs with depth. The best results were found with a two-layers model and uniform velocity within each layer.

The result of the inversion of the experimental dispersion curve of Love waves is presented in Fig. 11d along with the velocity-depth model deduced from the refraction study (Fig. 9d). All models which were fitted within the standard deviation were kept and considered acceptable. Results indicate a low velocity layer (125 m/s) at the top, over a thickness of 2 to 3 m (mean of 2.3 m) and which overlies levels with higher but badly resolved velocity (400 to 875 m/s). Vs within the dyke body is slightly lower than Vs obtained from the refraction study (145 m/s; Fig. 10b). The depth to the interface between the dyke and the bedrock (2 to 3 m) is also shallower than with Vs refraction (Fig. 11d), Vs image and drillings (3.5 to 5 m; Fig. 10b). Finally, Vs in the bedrock is also badly resolved and lower than what was provided

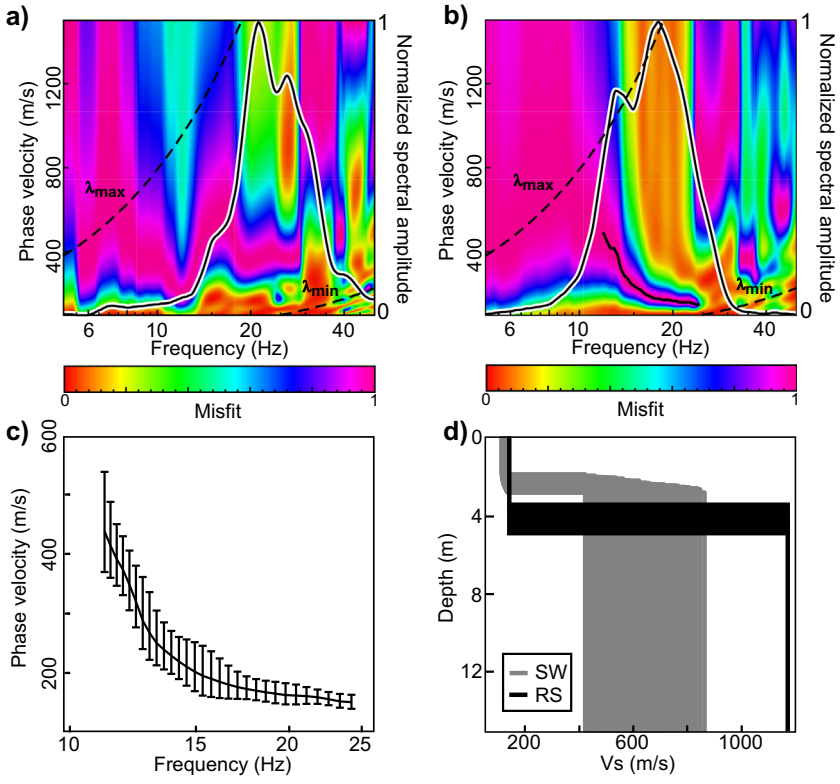

Fig. 11. Surface waves analysis along profile SP1. a) Rayleigh and b) Love waves phase velocity versus frequency for an endshot at 18 m along the profile and a group of 8 geophones between 34 and 48 m. The corresponding seismograms are shown in Fig. 9a (Rayleigh waves) and 9b (Love waves), respectively. The white line depicts the normalized spectral amplitude. The black line in Fig. 11b corresponds to the picked experimental dispersion curve for Love waves. c) Mean experimental Love waves dispersion curve for two endshots at 18 m and 64 m along the profile. Error bars correspond to the standard deviation. d) Vs profile (in grey) after inversion of the dispersion curve in Fig. 11c. SW: surface wave inversion; RS: refraction study (interpreted from data in Fig. 9b).

by the refraction study (1200 m/s; Fig. 11d) and by the Vs image (Fig. 10b). These discrepancies in velocity and thickness between, on the one hand, Vs refraction study and tomography and drillings and, on the other hand, Love waves inversion, could originate from the complex geometry of the dyke, with a complex surface morphology preventing the 1D approximation. These discrepancies could also originate from Vs lateral variations and from the dyke thickness along the profile, as observed along profile SP1 (Fig. 10b).

In summary, seismic results revealed a two-layer ground. Vs tomography allowed to image the base of the dyke between 3.5 m and 5 m depth along the seismic profile, in agreement with geotechnical data. The water table was detected, using P-wave analysis, at around 2.1 m, in agreement with hydrogeological data. Rayleigh surface waves showed to be inefficient, probably because of a strong 3D geometrical context. On the contrary, it was possible to invert Love waves but the results (both velocity and depth to the interface are underestimated) are not in full agreement with the geotechnical tests nor with the Vs image. Apart from the complex geometrical setting, this could also probably originate from lateral variations in Vs and in the thickness of the dyke.

4.2.2. Electrical resistivity tomography

Electrical Resistivity Tomography (ERT) results along profiles EP1 and EP2 (location in Fig. 2) are presented in Fig. 12a (EP1) and in Fig. 12b (EP2). They both indicate superficial levels with low resistivities (<70 Ω·m) over 3 to 5 m (EP1) and 2 to 5 m (EP2) height. These levels correspond to the dyke body and the resistivity values are consistent with a partially to fully saturated mixture of clays, silts and sands. The thickness is maximum in the centre of the profile. Below this depth, resistivity range between 100 and 300 Ω·m and suggests a saturated and more or less weathered marly limestone bedrock. These results are in agreement with the results from drillings, γ-ray logging and in situ geotechnical tests (Fig. 12). Within the bedrock, two low resistivity zones (from 55 to 70 m and from 110 m to the end of the profile) are observed. They could be indicative of a locally more intensely weathered substratum. The thick dashed line on profile EP1 (Fig. 12a) corresponds to the a priori information deduced from SH tomography (Fig. 10b). An inversion was conducted without this a priori information. It provided globally the same result. It can however be seen that the contrast between the dyke and the bedrock is much more sharp when this interface is used for the inversion.

Of particular interest is the difference in resistivity values between the two profiles. Fig. 12 shows that the dyke appears less resistive in EP2 (mean resistivity around 35 Ω·m) compared to EP1 (mean resistivity around 50 Ω·m). In the same way, the bedrock appears less resistive in profile EP2 (100–150 Ω·m) compared to EP1 (120–300 Ω·m). The water table was located at the same depth in boreholes d2 and d3 (4.5 m below dyke crest; Fig. 4) during ERT measurements. The water table was then sub-horizontal and should not drive to the observed differences in resistivity. In the same way, γ-ray values in boreholes d2 and d3 are comparable (around 60 c/s) and suggest that the dyke is here made of the same soil. Finally, these differences are also observed within the Jurassic bedrock (more resistive in EP1 than in EP2). The observed difference in resistivity between the two profiles does not seem to originate from the resistance measurements. It is more likely that this discrepancy originates from the differences in geometry (EP1 on the top of the dyke and EP2 along the road 1.5 m below the dyke crest). These differences might induce variations in the geometric factor k which are not taken into account by the analytical definition for an infinite half-space (Fargier et al., 2014).

4.3. Ambient vibrations monitoring

Fig. 13a presents seismograms of ambient vibrations recorded along profile SP1 (location in Fig. 2) in November 2010, before remediation works. Amplitudes are expressed with a common scale. It shows that four traces, located between 34 m and 40 m, have noise amplitudes much larger than the other ones. This location corresponds to the position of SEP1 (35.5 m) and LZ1 (34.5 m) along the profile (Fig. 2). This suggests that the leakages within the dam body generate significant vibrations which can be recorded at the surface of the dyke. Fig. 13b presents the same recordings (with the same amplitude scale) conducted in May 2011. The striking feature is that every trace has the same noise level, and also that traces between 34 m and 40 m along the profile have considerable reduced noise level after remediation works when compared to the recordings of November 2010 (Fig. 13a). This results suggest that remediation works significantly reduced the leakages within the dam body such that induced vibrations cannot be detected anymore. It also confirms that vibrations recorded in November 2010 between 34 m and 40 m originated from the water piping from LZ1 through the dam body.

Fig. 13c presents the superimposition of the maximum absolute amplitude of seismograms in Fig. 13a and b. It shows the lateral evolution of the maximum amplitude recorded at each geophone along profile SP1 during 1 min. It is expressed with a common normalized amplitude scale. The two most energetic traces are found at a distance of 34 m and

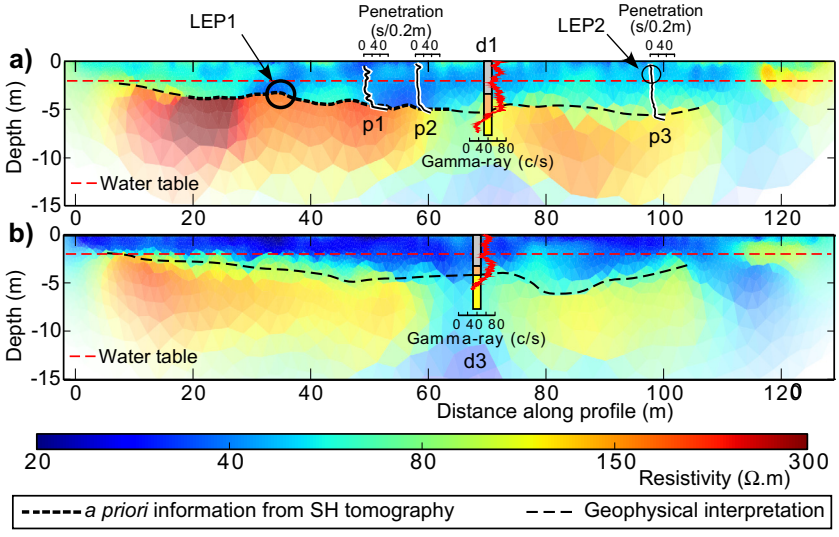

Fig. 12. Electrical Resistivity Tomography. The location of the profiles is indicated in Fig. 2. a) Profile EP1 conducted on the top of the dyke. b) Profile EP2 located along the road, around 1.5 m below the dam crest.

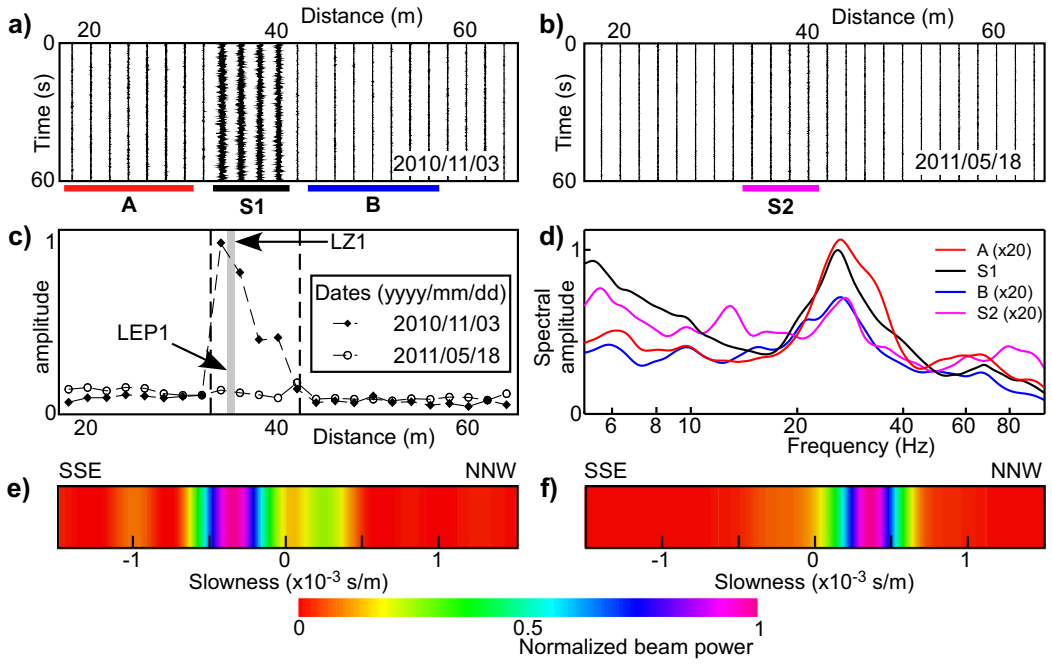

Fig. 13. Seismic noise monitoring with 4.5 Hz vertical geophones along profile SP1 (location in Fig. 2). a) Seismograms recorded the 03rd of November 2010, before remediation works. A, S1 and B: see Fig. 13d. b) Seismograms recorded the 18th of May 2011 after works; S2: see Fig. 13d. c) Maximum absolute amplitude recorded at each geophone and expressed with a common amplitude scale. d) Fourier spectra of the 4 groups of geophones A, S1, B and S2. The position of the groups along profile SP1 is detailed in Fig. 13a-b. The spectral amplitude is expressed with a normalized scale and a factor of 20 for A, B and S2. e) and f) wavenumber analysis (expressed in slowness) at a frequency of 25 Hz for A and B, respectively.

36 m. They are located immediately apart from the location of LZ1 (34.5 m) and PH1 (35.5 m) along the profile. However, it is possible to observe energetic vibrations for a distance of up to around 42 m along the profile. This suggests that the path of the leakage within the dam body might not be straightforward between SEP1 and LZ1, but rather tortuous. This spatial coverage along the profile (33–34 m to around 42 m) is materialized in Fig. 13c by two vertical dashed lines. In order to assess that the water flowing through the dam body is the source of these energetic vibrations, their direction of propagation was analysed. The seismic profile was first cut into 3 groups of geophones, assuming that the source is located between abscissa 33–34 m and around 42 m (the four most energetic seismograms, labelled S1 in Fig. 13a). Assuming a wave propagation from S1, 7 geophones towards the beginning of the profile (A in Fig. 13a) and 7 towards the end (B in Fig. 13a) were selected. The spectral amplitude of each group is presented in Fig. 13d. S1 shows a pronounced peak at 25 Hz, which can be interpreted as the central frequency of the vibrating source. The 2 groups A and B also show a distinct peak at this central frequency (Fig. 13d; a factor of 20 was applied to both amplitudes of A and B). The spectral analysis was also conducted for group S after remediation works. The seismograms are shown in Fig. 13b (the group of geophones is labelled S2) and the spectral curve is presented in Fig. 13d with a factor of 20 for the amplitude. It shows the presence of a peak with a central frequency of around 25 Hz but with a magnitude 20 times lower than for S1. This suggests that water still flows at the interface between the dam body and the bedrock, but with a very reduced magnitude. This is in agreement with field observations where the flow at LZ1 was evaluated at around 250 l/min before works and at around a few tens of l/min after works (see Section 2). Groups A and B were then analysed in the *f-k* domain, for a central frequency of 25 Hz, deduced from the previous spectral analysis. The results are presented in Fig. 13e (A) and f (B) and are expressed in terms of slowness. For A, the slowness is negative and suggests a wave propagation towards the beginning of profile SP1 (i.e. from right to left in Fig. 13e). On the contrary, the slowness is positive in the case of B (Fig. 13f), which indicates a propagation directed towards the end of profile SP1. These results indicate that wave propagation originates from below the group of geophones S1. They suggest that the leakage path within the dyke is located below these geophones. This is supported by visual observation conducted after the emptying of the canal. However, the analysis of slowness reveals unrealistic values, corresponding to velocities of 300–800 m/s and 300–650 m/s for A and B, respectively. However, these values can only be considered as apparent velocities. The source is located at depth, below the water table, and close to the groups of geophones: this experimental setup is located in the near-field and hence does not respect the condition of incident plane waves.

4.4. Seismic source localization

From previous section, it was shown that the water flow within the leakage path acts as a seismic source. Ambient vibrations recorded at the surface along profile SP1 might then contain information which could be used to track back the energy to its source. The algorithm defined in Section 3.2 was used on the 1 min-long signal for a wide set of initial parameter tests (β, time-window δ, inter-distance weights w) which were detailed in Section 3.2. The results of the localization of the seismic source along profile SP1 and at depth, before and after works, are presented in Fig. 14. Fig. 14a presents the results of parametric tests in terms of velocity bounds. The stability of the depth inversion was reached by using relatively high velocities (Vmax > 500 m/s). Below 500 m/s the algorithm focuses the solution on the lower limit of the half space. This high velocity, as well as the better residuals ε found for amplitude decay function of R^{-1}, suggest that the most energetic part of the signal generated by this leakage is most probably composed of body waves. Using a maximum velocity of 600 m/s on the data from November 2010 lead to a location of the source at X = 37.1 m and Z = 3.0 m (Fig. 14b). These values are very close to the observed locations (X = 35.5 m and Z = 3.4 m). The uncertainties are found to be 0.4 m both horizontally and vertically. Allowing the maximum velocity to increase up to 1000 m/s does not influence the horizontal location. The main effect is found on depth estimation. Using maximum velocities of 1000 m/s and 500 m/s lead to a source depth of 2.8 m and 3.3 m, respectively. This suggests that the retrieved depth is sensitive to the wave velocity but remains within the limits of the uncertainties.

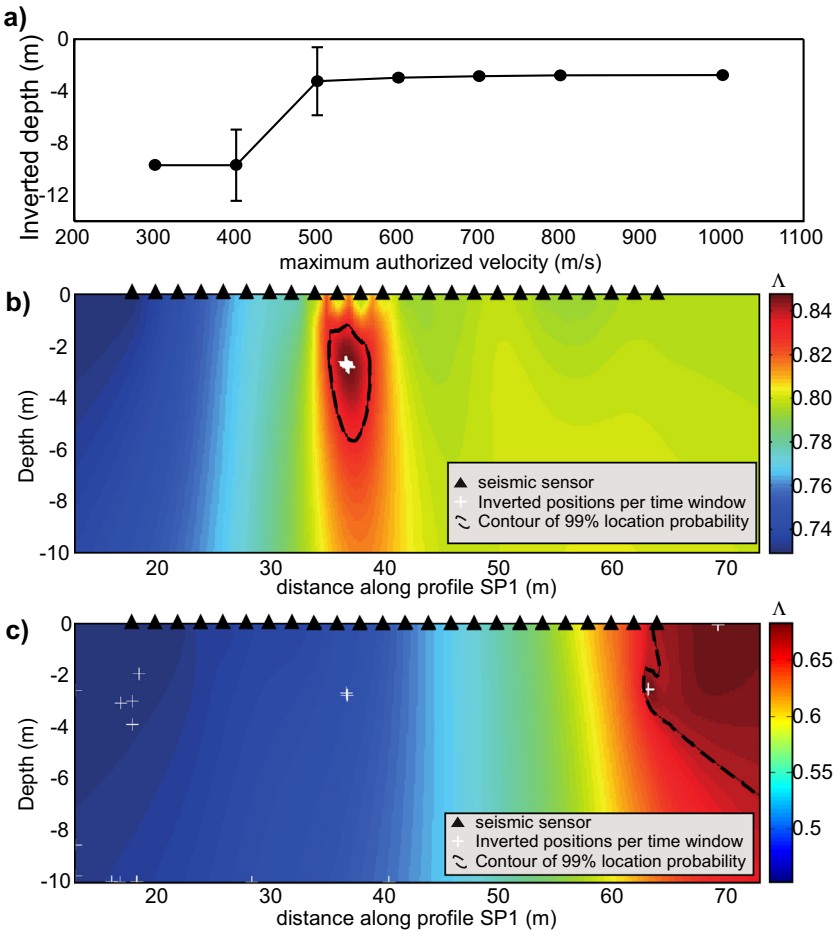

Fig. 14. Localization of the seismic source. a) Inverted depth as a function of the maximum velocity. b) and c) Probability Density Function (PDF) of the localization of the seismic source along profile SP1 in November 2010 (before remediation works) and in May 2011 (after remediation works), respectively. The white crosses represent the best locations inverted for each time window. The 99% PDF is showed as a black ellipsoid. Please note that the colorscale is not the same for Fig. 14b and c.

This confirms the robustness of the algorithm to determine the source depth.

In Fig. 14b, it is first observed that the series of localizations inverted per time-window (white cross) is more grouped than 99% of the location probability defined on the general distribution of Λ (black ellipsoid). Therefore, the location uncertainty is here defined as the standard deviation of the inverted locations over all the time-windows. The median and standard deviations of this time-series were computed as a function of the different parameters of the location process.

The same measurements were conducted along the same profile after remediation works, in May 2011. Results are presented in Fig. 14b. They show that no more seismic source can be located within the seismic network. Instead, the localization process shows a source coming from outside the network. Its precise localization is thus not possible, as shown by the large size of the 99% maximum contour. Moreover the maximum values of Λ are much lower than before remediation works (0.65 against 0.85). All these observations together show that the leakage does not produce detectable seismic signals anymore. It thus suggests that remediation works significantly reduced the water flow at this location.

5. Discussion

The comparison between the geotechnical and geophysical interpretation is presented in Fig. 15. Since no geophysical method was able to distinguish between the poorly contrasted units 1 and 2, they will further be referred to as a single unit (the dyke itself) in Fig. 15a. Vp tomography was strongly influenced by the presence of a water table (Fig. 10a) which was detected at a depth of around 2.3 m, in agreement with piezometric and tests results. The base of the dyke was therefore not detected (Fig. 15a), which is a strong limitation of this technique for canal dyke investigation. Vs tomography (Fig. 10b) and ERT (Fig. 12) were both able to precisely locate the base of the dyke along the profile (Fig. 15a). Furthermore, Vs tomography detected a low velocity zone at the top of the bedrock, between 35 m and 45 m along the profile, probably corresponding to a more or less intensively weathered part of the top of the bedrock. This zone corresponds to the location of SEP1/LZ1 (Figs. 2, 3). This suggests that the piping developed in a mechanically weakened zone at the interface between the base of the dyke and the top of the bedrock. This interpretation is consistent with findings by other authors who suggested that the contact between an embankment and the foundations is a preferential location for the development of internal erosion (Foster et al., 2000; Fell et al., 2003).

Surface waves were only recently applied to embankment dams characterization (Cardarelli et al., 2010; Karl et al., 2011; Cardarelli et al., 2014). The 1D hypothesis was numerically assessed for Rayleigh waves by Karl et al. (2011). These authors argued that the 1D assumption was valid for dykes with a width-to-height ratio over 4. On the study site, this ratio is around 3.5 and, consequently, the 1D assumption might not be respected. Our findings are in agreement with this statement. From the inversion of Love waves (Fig. 11d), the best ground model was chosen to conduct forward simulations. A two layers model with a dyke thickness of 2.3 m was chosen. Vp and Vs in the dyke (bedrock) were set to 400 (2000) m/s and 125 (500) m/s, respectively. A second model, with the same velocities but with a dyke

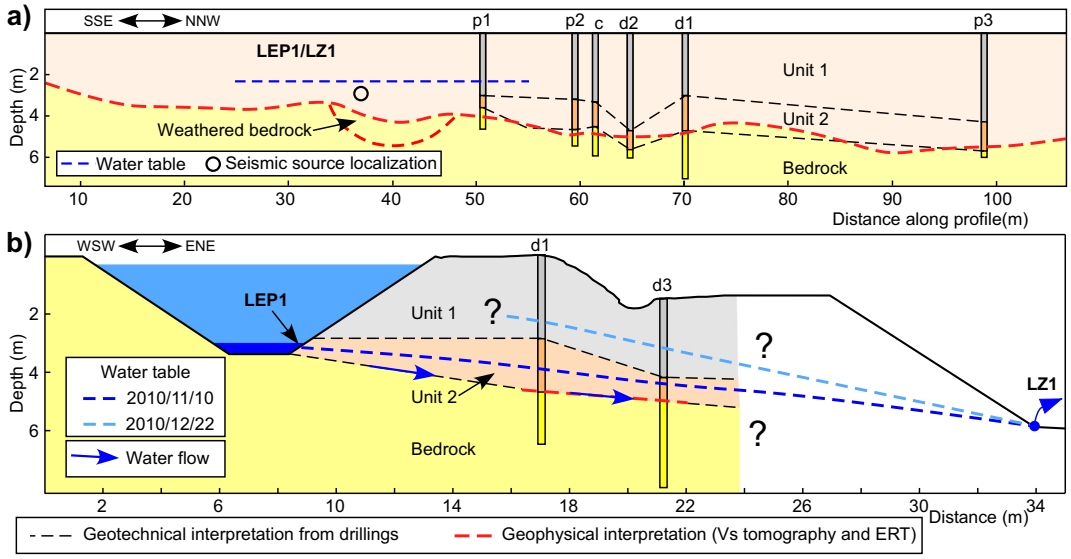

Fig. 15. Geotechnical model deduced from the geotechnical and geophysical interpretation. a) 2D section along profile EP1. b) 2D section perpendicular to the dyke.

thickness of 4 m, in agreement with drillings and tomographies, was also computed. The ground models were used as an input to compute the fundamental and first higher mode of Love waves dispersion curves. Results are exposed in Fig. 16 and are superimposed on the experimental *f-k* diagram of Fig. 11b. They suggest that the theoretical and experimental dispersion curves for the fundamental mode match well for a dyke thickness of 2.5 m and that it is the fundamental mode which propagates between frequencies of 12 Hz and 25 Hz (Fig. 16a). On the contrary, with a dyke thickness of 4 m (Fig. 16b) corresponding to the site condition, no theoretical dispersion curve matches the experimental one.

The theoretical dispersion curve of the fundamental and first higher mode of Rayleigh waves was computed using the same ground models. The results are depicted in Fig. 16b and show the forward calculations along with the experimental *f-k* diagram for a shot at 0 m along profile SP1 (same diagram as in Fig. 11c). They suggest that the experimental and theoretical data do not fit satisfyingly. This indicates that the experimental Rayleigh SW measurements might be perturbed by the particular surface morphological setting (below a width-to-height ratio of 4 according to Karl et al. (2011). However, this still does not explain why Love waves, contrarily to Rayleigh waves, and even if they provide an underestimation of both the depth to the bedrock and Vs in the dyke and the bedrock, do not appear as much perturbed. This effect still needs to be understood.

ERT was able to locate the base of the dyke along the whole profile. However, comparison of profiles EP1 and EP2 (Fig. 12) shows different resistivity values of both the dyke and the bedrock between the two profiles. Piezometric data indicate that the water table were at comparable depths and do not allow to explain this difference. In the same way, γ-ray values are identical between drillings (50 to 70 c/s; Fig. 12) and suggest that the clay content in the dyke body is identical. This discrepancy could then originate from the varying surface morphological context between the two profiles (EP1 at the top of the dyke and EP2 1.5 m below the dyke crest) which would influence the geometrical factor and, hence, the determined apparent resistivities. This effect has already been evaluated numerically and experimentally (Hennig et al., 2005; Sjödahl et al., 2006; Cho et al., 2014; Fargier et al., 2014). The influence of the location of the ERT profile along the dyke on resistivity measurements could be evaluated numerically. Further works might also allow to evaluate the possible influence of varying water levels into the canal on time-lapse resistivity monitoring conducted along the dyke.

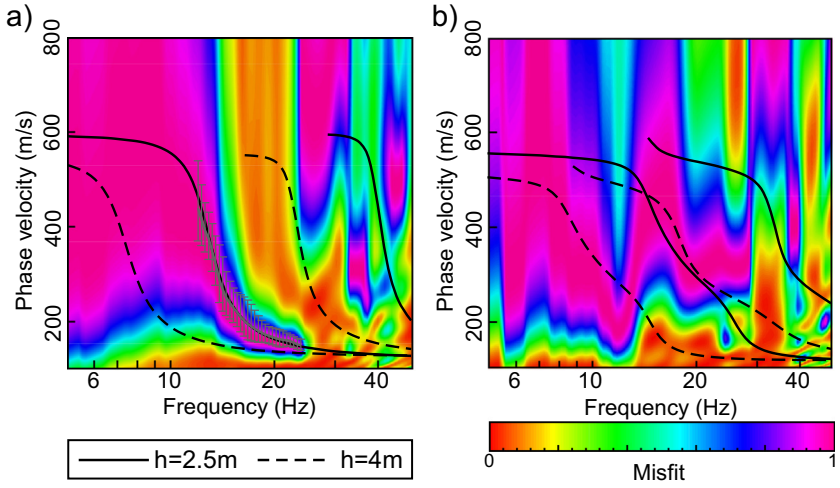

Fig. 16. Forward calculations of theoretical dispersion curves for the fundamental and the first higher mode of surface waves (black curves) for two heights of the dyke (2.5 m and 4 m). a) Love waves, with the experimental dispersion curve (Fig. 11b,c) in grey. b) Rayleigh waves with the experimental f-k diagram for a shot at 0 m along profile SP1 (Fig. 11a).

A simple visual analysis of the seismograms acquired before works (Fig. 13a) allowed to quickly and roughly locate the position of the leakage along the profile. The combination of phase and amplitude of seismic waves using a beam-forming algorithm allows to locate the source at depth. The best locations are found for seismic velocities relatively high (between 600 and 1000 m/s) showing that the origin of the generated waves are certainly body waves. Moreover the S-wave profile (Fig. 10b) displays velocities of 150 m/s in the top layer and 600 m/s below the leakage interface, showing that S-waves travelling with velocities higher than 600 m/s is very unlikely. This suggests that the most energetic waves recorded by the seismometers are certainly P-waves. Based on this observation, a 2-layers model could be implemented in the future to better locate the source. This is however beyond the scope of this work which simply aimed at locating the source without any a priori informations.

The physical processes of this seismic noise generation has been little studied. Planès et al. (2015) showed that increase in seismic ambient vibrations is linked to increase of pore water pressure. They however focused very little on the mechanism of seismic wave generation. Studies realized on other flows like rivers show that seismic noise generation in the frequency 1–100 Hz is generated by two processes: (1) bedload transport flux (Tsai et al., 2012), (2) turbulent water flow (Gimbert et al., 2014). In the pipe erosion situation, the fine granulometry of eroded particles could probably not generate a seismic noise comparable to the bedload transport in rivers. The turbulence level in the leakage pipes could be estimated by computing the order of magnitude of Reynolds number: it could be estimated to 20,000 for the leakage zone LZ1 (with a pipe diameter of 0.2 to 0.3 m and a flow rate of 250 l/min) and around 2000 for SEP2 (with a pipe diameter of 0.2 to 0.3 m and a flow rate of 25 l/min). The turbulence is then moderate but well established for LZ1 and of a much lower level (and potentially in the range of laminar or transition domain) in LZ2. The flow turbulence is most probably the main source of seismic signal. The reduced noise recorded from the second leakage can then be explained by the lower turbulence level. Moreover, turbulent transport in an open river has been shown to be generated at frequency around or lower than 10 Hz (Gimbert et al., 2014) lower than for bedload transport, which corresponds to the frequencies of maximum energy recorded here.

These hypothesis were confirmed by the analysis of ambient vibrations in terms of direction of propagation. It was shown that seismic waves propagated from LZ1 towards both ends of profile SP1 (Fig. 13e and f). The second leakage zone LZ2 was not possible to locate, probably because of a too low energetic content and because the main propagation in the seismograms came from source LZ1. These results however confirm that the water flowing through the leakage zone acts as a seismic source. Ambient vibration measurements were then processed accordingly using beam-forming techniques. The results provided a location at surface (around 37 m $\pm$ 0.4 m) and at depth (3 m $\pm$ 0.4 m) in very good agreement with field observations (Fig. 14c). These results need however to be confirmed over other areas of leakages, and with other experimental settings. The experimental set up was originally not fully designed to process such data. Much longer time series are needed to obtain thorough correlations (Planès et al., 2015). Also, the type of waves (body waves and/or surface waves) which propagate within the dyke close and far from the source must be confirmed to use a constrained velocity model. Finally, it must be stressed out that similar measurements conducted above LZ2 along profile SP2 did not allow to detect a seismic energetic content and to locate the leakage within the dyke. This might be caused by a low energetic content of the water flow or by a seismic signature of the leakage blinded by the LZ1 leakage. Further works might allow to evaluate the critical amplitude needed for detecting a water flow within an earth dyke. These results were obtained with only 1 min of ambient vibrations. They are however promising and might help to efficiently and quickly locate leakage paths within an earth dyke prone to internal erosion and piping phenomena.

6. Conclusion

This paper investigated the combined use of extensive geotechnical, hydrogeological and geophysical techniques to assess the condition of a small earth dyke with a permanent hydraulic head. The results showed a good agreement between the geophysical imaging techniques (refraction and electrical resistivity tomography) and the geotechnical data to detect the depth to the bedrock and its lateral variations. It appeared that surface waves might not be fully adapted to investigate such a small dyke because of the particular geometry of the structure, non-respectful of the 1D assumption. Furthermore, depth and velocity discrepancies were observed on the 1D Vs profiles retrieved from Love waves inversion. These differences might be caused by the particular geometrical setting of this dyke. Further numerical studies might allow to better understand wave propagation within these highly complex structures.

The use of these classical prospecting techniques however did not allow to directly locate the two leakages. The analysis of ambient vibration time series suggests that it is feasible to quickly locate, at surface, the position of an energetic water flow (LZ1) through the dyke. Furthermore, a beam-forming technique was adapted to locate a pipe at depth. The promising results allowed to locate the main leakage with an uncertainty of 0.4 m. However, the method did not succeed to locate the second piping, because of a too small signal-to-noise ratio. Further research must be performed to study the limits of this detection/localization method, in particular the flow limit of the detectable leakage. To achieve this goal, future works should focus on understanding the physical process linked with the generation of the seismic signal in the leakage zone. Longer time-series might have allowed to detect the presence of this internal erosion zone. Further numerical and experimental works will help to evaluate the conditions necessary to detect water flows caused by internal erosion within dykes, and to monitor their evolution with time.

Acknowledgements

This work was supported by the French IFSTTAR-CEREMA DOFEAS Program. The authors thank Cécile Cornou, Bertrand Guillier and Marc Wathelet (ISTerre) for their help with surface waves processing and inversion. Christophe Voisin (ISTerre) is acknowledged for discussions about the results and the manuscript. The authors thank Dr. Walid *Al*-Fares and an anonymous reviewer for their comments which helped to improve the manuscript.

References

Aki, K., Richards, P.G., 1980. Quantitative Seismology: Theory and Methods. W. H. Freeman, New York, USA.

Antoine, R., Fauchard, C., Fargier, Y., Durand, E., 2015. Detection of leakage areas in an earth embankment from GPR measurements and permeability logging. Int. J. Geophys. 2015:610172. http://dx.doi.org/10.1155/2015/610172.

Bogoslovsky, V.A., Ogilvy, A.A., 1970. Natural potential anomalies as a quantitative index of the rate of seepage from water reservoirs. Geophys. Prospect. 18, 261–268.

Bolève, A., Janod, F., Revil, A., Lafon, A., Fry, J.-J., 2011. Localization and quantification of leakages in dams using time-lapse self-potential measurements associated with salt tracer injection. J. Hydrol. 403:242–252. http://dx.doi.org/10.1016/j.jhydrol.2011.04.008.

Bolève, A., Vandemeulebrouck, J., Grangeon, J., 2012. Dyke leakage localization and hydraulic permeability estimation through self-potential and hydro-acoustic measurements: self-potential 'abacus' diagram for hydraulic permeability estimation and uncertainty computation. J. Appl. Geophys. 86:17–28. http://dx.doi.org/10.1016/j.jappgeo.2012.07.007.

Bouiller R, Arène J, Delfour J & Lemière B (1990) Carte géologique de la France à 1/50000: Charlieu (feuille 648), BRGM, Orléans, France

Cardarelli, E., Cercato, M., Donno, G.D., 2014. Characterization of an earth-filled dam through the combined use of electrical resistivity tomography, P- and SH-wave seismic tomography and surface wave data. J. Appl. Geophys. 106:87–95. http://dx.doi.org/10.1016/j.jappgeo.2014.04.007.

Cardarelli, E., Cercato, M., Filippo, G., 2010. Geophysical investigation for the rehabilitation of a flood control embankment. Near Surf. Geophys. 8:287–296. http://dx.doi.org/10.3997/1873-0604.2010018.

Carlsten, S., Johansson, S., Wörman, A., 1995. Radar techniques for indicating internal erosion in embankment dams. J. Appl. Geophys. 33:143–156. http://dx.doi.org/10.1016/0926-9851(95)90037-3.

Cho, I.-K., Yeom, J.-Y., 2007. Crossline resistivity tomography for the delineation of anomalous seepage pathways in an embankment dam. Geophysics 72:G31–G38. http://dx.doi.org/10.1190/1.2435200.

Cho, I.-K., Ha, I.-S., Kim, K.-S., Ahn, H.-Y., Lee, S., Kang, H.-J., 2014. 3D effects on 2D resistivity monitoring in earth-fill dams. Near Surf. Geophys. 12:73–81. http://dx.doi.org/10.3997/1873-0604.2013065.

Clayton, C.R.I., Matthews, M.C., Simons, N.E., 1995. Site Investigation. second ed. Blackwell Publishing, Oxford, England.

Fargier, Y., Lopes, S.P., Fauchard, C., Francois, D., Côte, P., 2014. DC-electrical resistivity imaging for embankment dike investigation: a 3D extended normalisation approach. J. Appl. Geophys. 103:245–256. http://dx.doi.org/10.1016/j.jappgeo.2014.02.007.

Fauchard, C., Mériaux, P., 2007. Geophysical and Geotechnical Methods for Diagnosing Flood Protection Dikes. Editions Quae, Paris, France.

Fell, R., Wan, C.F., Cyganiewicz, J., Foster, M., 2003. Time for development of internal erosion and piping in embankment dams. J. Geotech. Geoenviron. Eng. 129:307–314. http://dx.doi.org/10.1061/(ASCE)1090-0241(2003)129:4(307).

Foster, M., Fell, R., Spannagle, M., 2000. The statistics of embankment dam failures and accidents. Can. Geotech. J. 37:1000–1024. http://dx.doi.org/10.1139/t00-030.

Gimbert, F., Tsai, V.C., Lamb, M.P., 2014. A physical model for seismic noise generation by turbulent flow in rivers. J. Geophys. Res. Earth Surf. 119:2209–2238. http://dx.doi.org/10.1002/2014JF003201.

Günther, T., Rücker, C., 2006. A New Joint Inversion Approach Applied to the Combined Tomography of DC Resistivity and Seismic Refraction Data. 19th EEGS Symposium on the Application of Geophysics to Engineering and Environmental Problems, 2–6 April, Seattle, USA.

Günther, T., Rücker, C., Spitzer, K., 2006. Three-dimensional modelling and inversion of DC resistivity data incorporating topography - II. Inversion. Geophys. J. Int. 166: 506–517. http://dx.doi.org/10.1111/j.1365-246X.2006.03011.x.

Hennig, T., Weller, A., Canh, T., 2005. The effect of dike geometry on different resistivity configurations. J. Appl. Geophys. 57:278–292. http://dx.doi.org/10.1016/j.jappgeo.2005.03.001.

Ikard, S., Rittgers, J., Revil, A., Mooney, M., 2015. Geophysical investigation of seepage beneath an earthen dam. Groundwater 53:238–250. http://dx.doi.org/10.1111/gwat.12185.

Karl, L., Fechner, T., Schevenels, M., Francois, S., Degrande, G., 2011. Geotechnical characterization of a river dyke by surface waves. Near Surf. Geophys. 9, 515–527.

Kim, J.-H., Yi, M.-J., Song, Y., Jee Seol, S., Kim, K.-S., 2007. Application of geophysical methods to the safety analysis of an earth dam. J. Environ. Eng. Geophys. 12: 221–235. http://dx.doi.org/10.2113/JEEG12.2.221.

Lacroix, P., Helmstetter, A., 2011. Location of seismic signals associated with microearthquakes and rockfalls on the Séchilienne landslide, French alps. Bull. Seismol. Soc. Am. 101:341–353. http://dx.doi.org/10.1785/0120100110.

Lacroix, P., Grasso, J.-R., Roulle, J., Giraud, G., Goetz, D., Morin, S., Helmstetter, A., 2012. Monitoring of snow avalanches using a seismic array: location, speed estimation, and relationships to meteorological variables. J. Geophys. Res. Earth Surf. 117: F01034. http://dx.doi.org/10.1029/2011JF002106.

Minsley, B.J., Burton, B.L., Ikard, S., Powers, M.H., 2011. Hydrogeophysical investigations at hidden dam, Raymond, California. J. Environ. Eng. Geophys. 16:145–164. http://dx.doi.org/10.2113/JEEG16.4.145.

Nelder, J.A., Mead, R., 1965. A simplex method for function minimization. Comput. J. 7, 308–313.

Niederleithinger, E., Weller, A., Lewis, R., 2012. Evaluation of geophysical techniques for dike inspection. J. Environ. Eng. Geophys. 17:185–195. http://dx.doi.org/10.2113/JEEG17.4.185.

Ogilvy, A.A., Ayed, M.A., Bogoslovsky, V.A., 1969. Geophysical studies of water leakages from reservoirs. Geophys. Prospect. 17:36–62. http://dx.doi.org/10.1111/j.1365-2478.1969.tb02071.x.

Planès, T., Mooney, M.A., Rittgers, J.B.R., Parekh, M.L., Behm, M., Snieder, R., 2015. Time-lapse monitoring of internal erosion in earthen dams and levees using ambient seismic noise. Geotechnique http://dx.doi.org/10.1680/jgeot.14.P.268.

Reiffsteck, P., Dorbani, B., Haza-Rozier, E., Fry, J.-J., 2010. A New Hydraulic Profiling Tool Including CPT Measurements. Proceedings of the 2nd International Symposium on Cone Penetration Testing CPT'10.

Rittgers, J., Revil, A., Planès, T., Mooney, M., Koelewijn, A., 2015. 4-D imaging of seepage in earthen embankments with time-lapse inversion of self-potential data constrained by acoustic emissions localization. Geophys. J. Int. 200:758–772. http://dx.doi.org/10.1093/gji/ggu432.

Royet, P., Palma-Lopes, S., Fauchard, C., Mériaux, P., Auriau, L., 2013. Rapid and Costeffective Dike Condition Assessment Methods: Geophysics and Remote Sensing.

Rücker, C., Günther, T., Spitzer, K., 2006. Three-dimensional modelling and inversion of DC resistivity data incorporating topography - I. Modelling. Geophys. J. Int. 166: 495–505. http://dx.doi.org/10.1111/j.1365-246X.2006.03010.x.

Sjödahl, P., Dahlin, T., Johansson, S., 2009. Embankment dam seepage evaluation from resistivity monitoring data. Near Surf. Geophys. 7:463–474. http://dx.doi.org/10.3997/1873-0604.2009023.

Sjödahl, P., Dahlin, T., Johansson, S., Loke, M., 2008. Resistivity monitoring for leakage and internal erosion detection at Hallby embankment dam. J. Appl. Geophys. 65:155–164. http://dx.doi.org/10.1016/j.jappgeo.2008.07.003.

Sjödahl, P., Dahlin, T., Zhou, B., 2006. 2.5D resistivity modeling of embankment dams to assess influence from geometry and material properties. Geophysics 71: G107–G114. http://dx.doi.org/10.1190/1.2198217.

Socco, L.V., Strobbia, C., 2004. Surface-wave method for near-surface characterization: a tutorial. Near Surf. Geophys. 2, 165–185.

Telford, W.M., Geldart, L.P., Sheriff, R.E., 1990. Applied Geophysics, 2nd. Cambridge University Press, Cambridge, UK.

Tsai, V.C., Minchew, B., Lamb, M.P., Ampuero, J.-P., 2012. A physical model for seismic noise generation from sediment transport in rivers. Geophys. Res. Lett. 39, L02404. http://dx.doi.org/10.1029/2011GL050255.

Ursat, P., 1992. *Le* Perméafor. Appareillage de diagraphie de perméabilité. Bull. Lab. Ponts Chaussées 178, 19–26.

Wathelet, M., 2008. An improved neighborhood algorithm: parameter conditions and dynamic scaling. Geophys. Res. Lett. 35, L09301. http://dx.doi.org/10.1029/2008GL033256.

Wathelet, M., Jongmans, D., Ohrnberger, M., 2004. Surface-wave inversion using a direct search algorithm and its application to ambient vibration measurements. Near Surf. Geophys. 2, 211–221.

Weller, A., Canh, T., Breede, K., Vu, N.T., 2006. Multi-electrode measurements at Thai Binh dikes (Vietnam). Near Surf. Geophys. 4:135–143. http://dx.doi.org/10.3997/1873-0604.2005039.

Weller, A., Lewis, R., Canh, T., Möller, M., Scholz, B., 2014. Geotechnical and geophysical long-term monitoring at a levee of Red River in Vietnam. J. Environ. Eng. Geophys. 19:183–192. http://dx.doi.org/10.2113/JEEG19.3.183.

Xu, X., Zeng, Q., Li, D., Wu, J., Wu, X., Shen, J., 2010. GPR detection of several common subsurface voids inside dikes and dams. Eng. Geol. 111:31–42. http://dx.doi.org/10.1016/j.enggeo.2009.12.00.